Biomimetic Zirconia

Subjects: Materials Science, Biomaterials

Contributor: Juri Saruta

Bio-inspired or biomimetic design of biomaterials presents new possibilities for developing implantable devices with enhanced biocompatibility and novel functions.

bone-implant integration Y-TZP dental and orthopedic implant

1. Introduction

Bio-inspired or biomimetic design of biomaterials presents new possibilities for developing implantable devices with enhanced biocompatibility and novel functions [1][2][3][4][5][6][7][8]. No study has yet reported a potential application of biomimetic surface morphology, particularly at the nano-level, to endosseous implants for commercial use in the fields of dental and orthopedic surgery [9][10][11][12][13][14][15][16][17][18][19][20]. Most of the advancements thus far in implant surface design to improve their ability to integrate with bone can be characterized as development of micro-topography to enhance osteoblastic function [21][22][23][24][25][26][27][28][29][30][31][32]. Specifically, micro-scale roughness, ranging from 0.5 µm to 5 µm, made by various chemical and physical treatments has been shown to successfully promote osteoblastic differentiation, thereby leading to faster and firmer bone integration than a machined-smooth surface [22][23][25][28][30][31]. A major challenge remains unsolved with respect to how distinct meso- (10 to 500 µm) and nano-scale surface topography can be created, and more importantly, the osteoblastic reaction to these scales of morphology/roughness is largely untested. Establishing a technological platform and accompanying design strategy on an experimental yet scalable manufacturing level would provide an initial solution for these important outstanding questions in the field.

A recent laser technology advancement made a breakthrough in simultaneous creation of meso- and nano-scale topography on zirconia [20]. Zirconia, made with yttria-stabilized tetragonal zirconia polycrystal (Y-TZP), is an allergy-free implantable material which is biocompatible with bone [20][33]. Optimizing conditions for the solid-state laser etching has enabled the engraving of meso-scale grooves with unique nanostructures upraised from their surfaces [20]. It was demonstrated that the width and depth of these meso-scale grooves can be controlled. The next step is to harness the technology for a novel surface design to further improve cellular and tissue reaction. For application to dental and orthopedic implants, a specific goal is to enhance bone–implant integration. A possible strategy from a mechanical perspective is to effectively increase the surface area of the implant and also the mechanical interlocking between the implant and bone, and we hypothesized that meso-scale texture holds a key to accomplishing this strategy. From a biological perspective, we hypothesized that the simultaneous presence of optimized meso-scale and nano-scale textures would promote osteoblastic differentiation, and furthermore, that if the nano-texture could create a bio-inspired local environment, it would be even more effective.

2. Creation of Bio-Inspired Meso-/Nano-Scale Hybrid Textured Zirconia

We attempted to create zirconia surfaces with cactus-like meso-scale spikes and nano-scale architecture using crisscrossing solid-state laser etching, as illustrated in **Figure 1**. The meso-scale spikes were designed with 60 μm width and five different heights of 20, 30, 40, 60, and 80 μm. Zirconia experimental samples in cylindrical and disk forms were made from yttria-stabilized tetragonal zirconia polycrystal (Y-TZP) (**Figure 2**A). The zirconia samples roughened through laser etching appeared to reflect less light than polished-smooth zirconia. **Figure 2**B (top images) shows low-magnification SEM images of zirconia cylinders with different meso-spike heights created by laser etching as well as the polished-smooth zirconia without laser etching. Laser-etched zirconia samples exhibited uniform, even, and seamless formation of spikes all over their circumference, regardless of the spike height. High-magnification images of these zirconia cylinders vividly revealed the formation of cactus-like spikes with consistent size and height, and in perfect lattice alignment (bottom images in **Figure 2**B). By controlling laser conditions, meso-scale spikes of gradually increased height were successfully created, while the width was fixed to approximately 60 μm. Even higher-magnification images revealed the formation of randomly shaped, densely networked nanostructures all over the surfaces of spikes of all heights; the nano-architecture resembled trabecular bone (**Figure 2**C). The trabeculae-like structures were 100 to 400 nm in size and appeared assembled and upraised from the base zirconia.

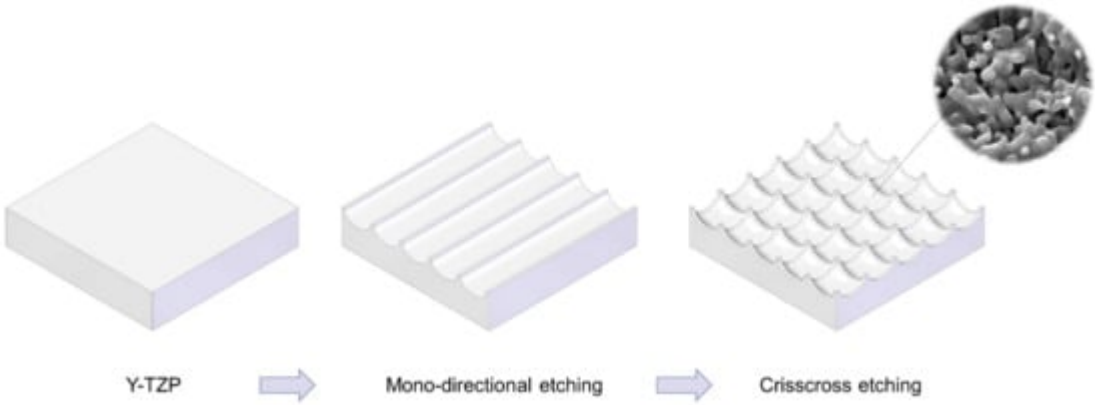

Figure 1. Schematic illustration of design strategy used to create cactus-inspired meso-scale spikes. Crisscrossing lattice grooves are engraved by vertical and horizontal laser etching. The grooves are hemispherical, leaving unengraved areas projecting as spikes. The width and depth of the grooves are controllable; the width was fixed at 60 μm in the present study, while the depth was varied in 5 increments from 20 to 80 μm.

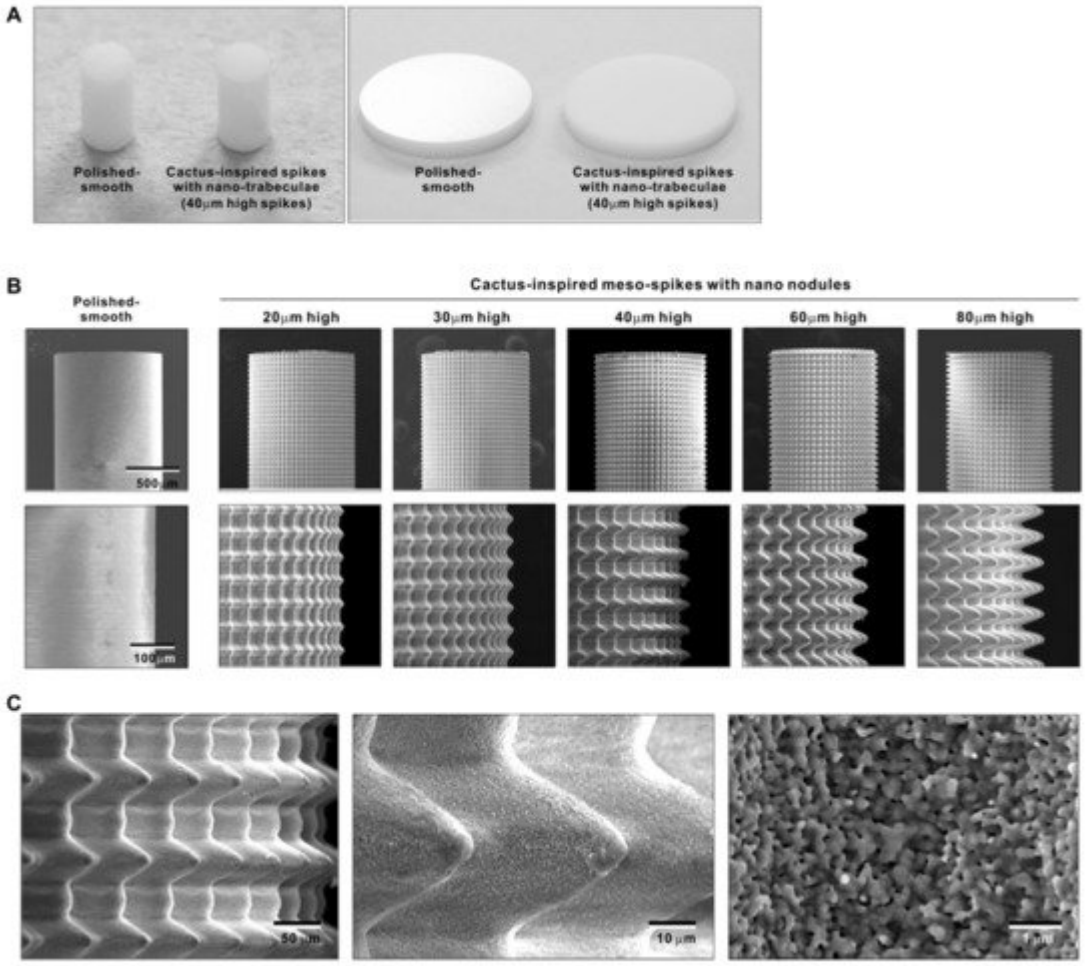

Figure 2. Creation of bio-inspired meso- and nano-scale hybrid textured zirconia. (**A**) Photographs of experimental zirconia samples made in cylinder and disk forms. Shown are a polished-smooth surface and a 40 μm-high spiked surface as a representative laser-etched zirconia sample. (**B**) Low-magnification SEM images of the polished cylinder zirconia and the meso- and nano-scale textured cylindrical zirconia with various heights of meso-spikes. The meso-scale spikes resembled cactus prickles. (**C**) High-magnification SEM images of the meso- and nano-scale textured zirconia with 40 μm-high spikes, vividly capturing the co-existence of cactus-inspired meso-spikes and nano-scale interwoven architecture resembling trabecular bone.

3. Quantitative Assessment of Surface Roughness of Bio-Inspired Meso-/Nano-Scale Hybrid Textured Zirconia

We continued analyzing the meso-/nano-scale hybrid textured zirconia. Three-dimensional images captured 3-D projection of the meso-scale spikes with heights incrementally increased from 20 to 80 μm (**Figure 3**A). Zoomed-in views of the meso-spiked surfaces showed that the laser etching produced highly controlled, smooth outlines oscillating from peaks to valleys (**Figure 3**B,C).

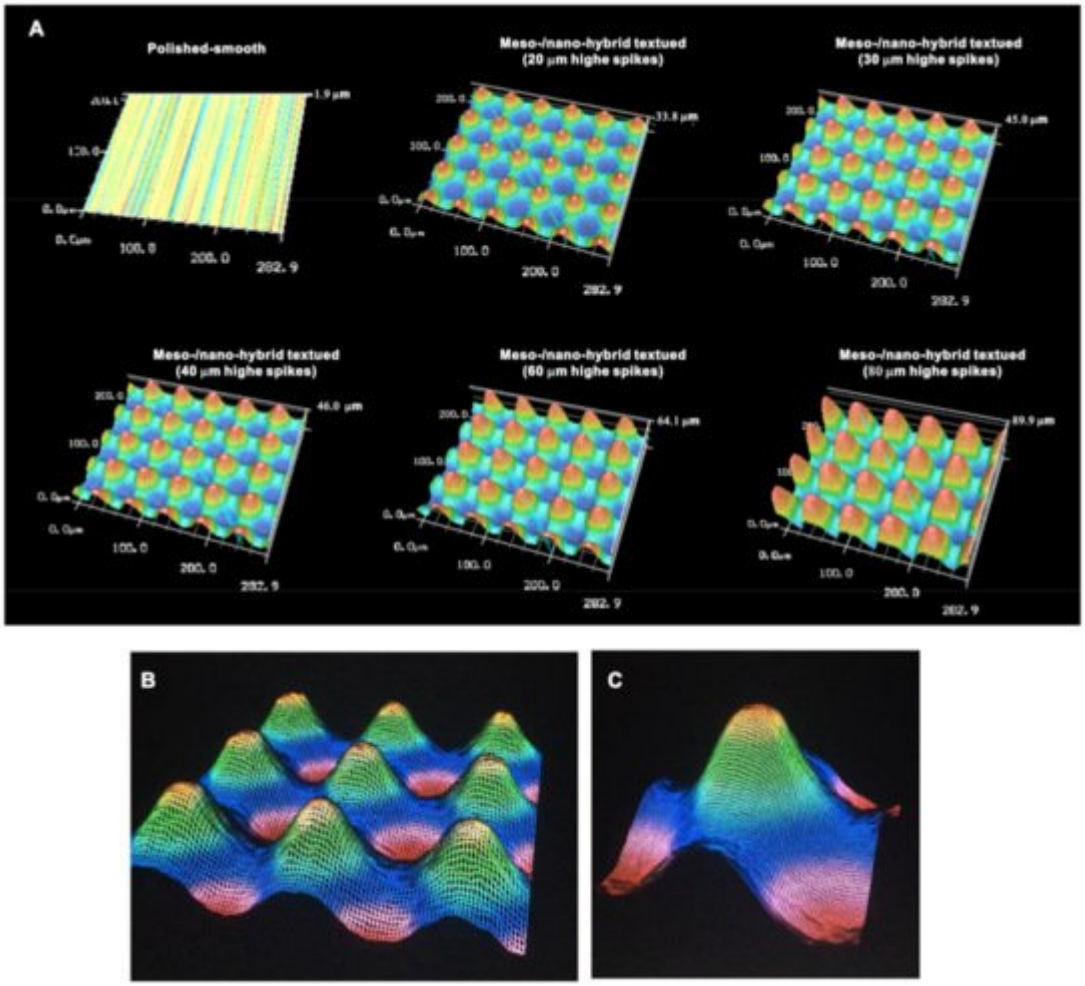

Figure 3. Three-dimensional profiles of the bio-inspired meso- and nano-scale hybrid textured zirconia. (**A**) Three-dimensional images of the polished zirconia and the meso- and nano-scale textured zirconia with various heights of meso-spikes. (**B**,**C**) Close-up images of the 40 μm-high meso-spikes, depicting precise and smooth transitions from peaks to valleys.

Cross-sectional profiling along the line connecting spike peaks confirmed smooth, oscillating curves of spikes and valleys (**Figure 4**A). The width of a spike was stable at approximately 60 μm for all height variations. The heights of spikes measured by profiling and the average peak-to-valley roughness (Sz) nearly matched the anticipated heights, with the measured heights of 23.1, 32.3, 42.5, 62.5, and 85.5 μm for the anticipated heights of 20, 30, 40, 60, and 80 μm, respectively (**Figure 4**A,B). There was a very high correlation between the measured spike height (Sz) and the anticipated height (R^2 = 0.9975; **Figure 4**B). The coefficient of variation for Sz was less than 1.5% for 30, 40, 60, and 80 μm-high spikes and near 1.0% for 40 and 60 μm-high spikes (**Figure 4**C). These data indicate the precision and reproducibility of the surface texturing process. Sz, average roughness (Sa), and surface area increased dramatically with the addition of meso-spikes and further increased in proportion to the incremental height increase of the meso-spikes (**Figure 4**D). Of significance, Sa exceeded 5.0 μm when the spike height was 30 μm or higher, followed by a further increase to over 15 μm. The surface areas of samples with 20, 30, and 40 μm-high spikes were more than twice that of the polished surface and increased to 4.43 times that of the polished surface with 80 μm-high spikes.

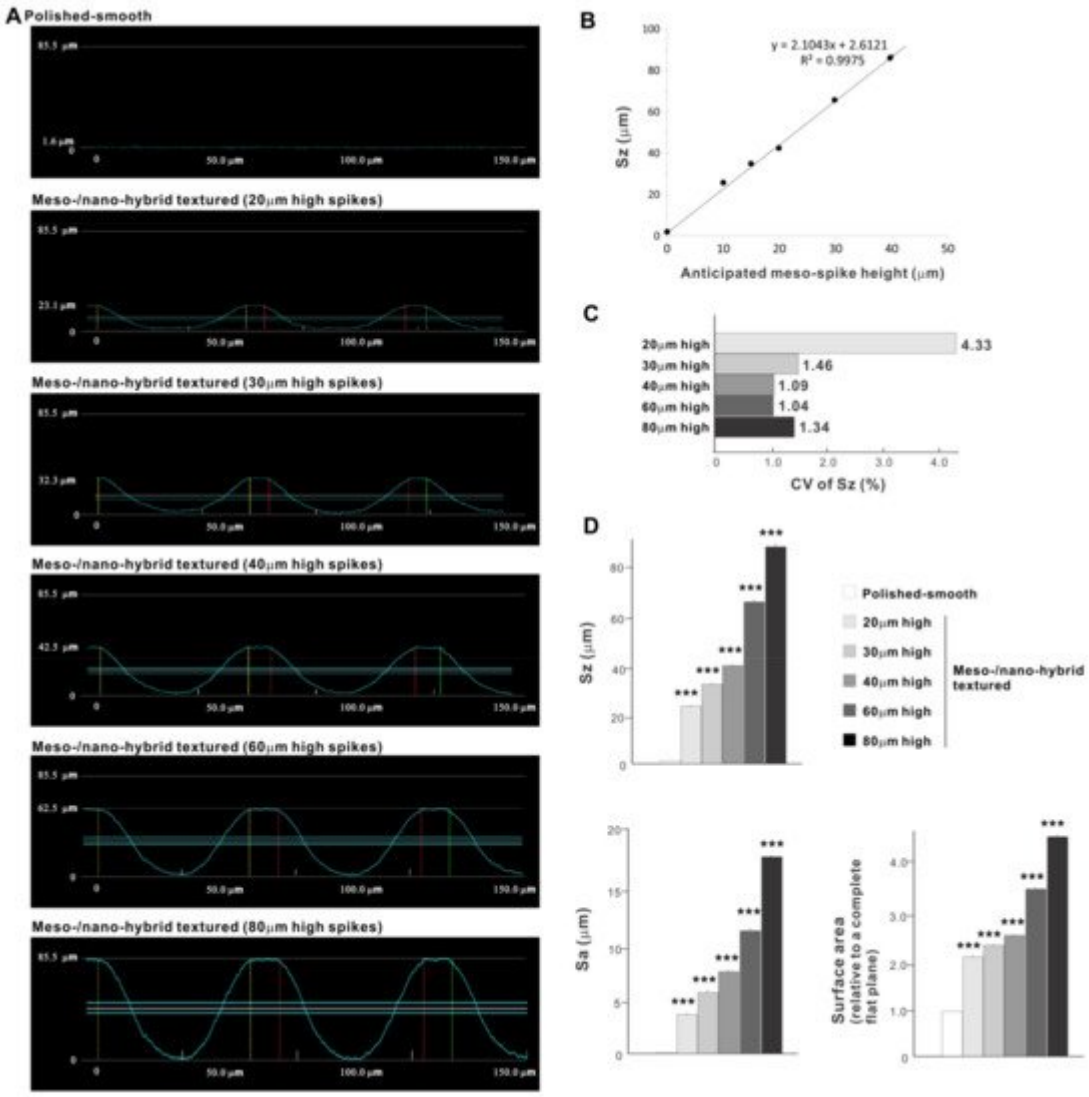

Figure 4. Quantitative surface analyses of the bio-inspired meso-/nano-scale hybrid textured zirconia. (**A**) Cross-sectional profile curves of the polished-smooth zirconia and the meso-/nano-scale textured zirconia with various heights of meso-spikes. (**B**) Sz (peak-to-valley roughness) plotted against the estimated/planned height of meso-scale spikes, showing a near-perfect linear correlation. (**C**) Coefficient of variation (CV) of Sz for different height designs of meso-scale spikes. CV (%) = (SD/Mean) × 100. (**D**) Quantitative topographical evaluations; Sz, Sa (average roughness), and surface area. *** $p < 0.001$, statistically significant difference compared with a polished surface.

4. Osteoblast Attachment and Proliferation on Meso-/Nano-Scale Hybrid Textured Zirconia

In a quest to optimize a zirconia surface for the promotion of bone–implant integration, we cultured osteoblasts on meso-/nano-scale hybrid textured zirconia with various spike heights as well as on a polished-smooth zirconia surface. The number of osteoblasts attached to the zirconia surfaces was evaluated during the initial stage of culture on day 2. All hybrid-textured zirconia surfaces showed a significantly lower number of attached cells than on

the polished surface (**Figure 5**), and among these, the surface with 20 μm-high spikes showed the lowest number of attached cells. There were no statistically significant differences among the rest of the hybrid-textured zirconia samples.

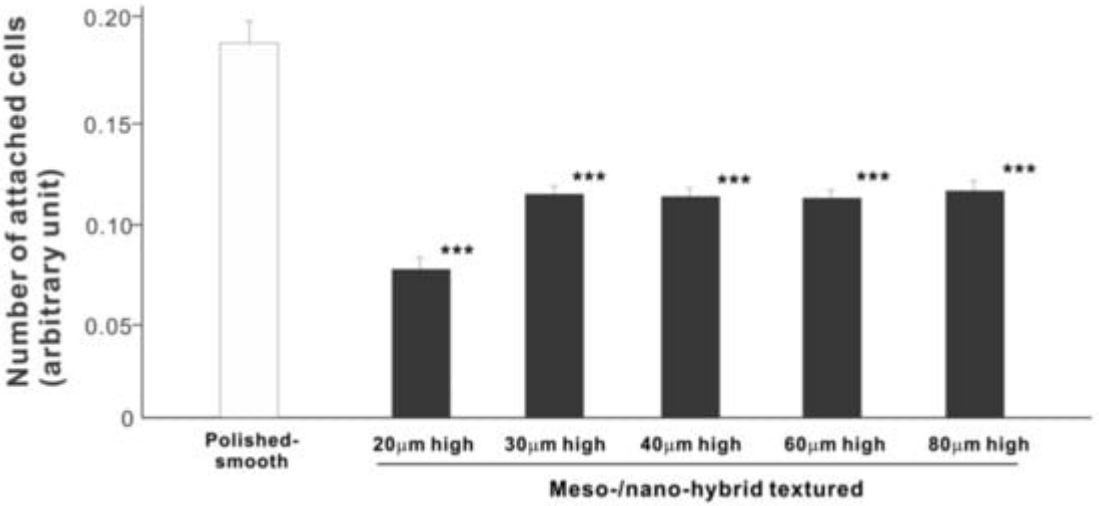

Figure 5. Attachment of osteoblasts to differently textured zirconia surfaces during the initial stage of culture, evaluated by WST-1 assay on day 2. *** $p < 0.001$, statistically significant difference compared with a polished surface.

We then examined the ability of the zirconia samples to support cell proliferation by measuring the density of cells on day 5 of culture (**Figure 6**). The cell density on all hybrid-textured zirconia samples was significantly lower than on the polished surface. The difference between the polished surface and hybrid surfaces was diminished compared to the initial cell attachment evaluated on day 2. A decreasing trend was found on the hybrid surfaces with higher spikes, although there was no significant difference among the surfaces with 20, 30, 40, and 60 μm-high spikes.

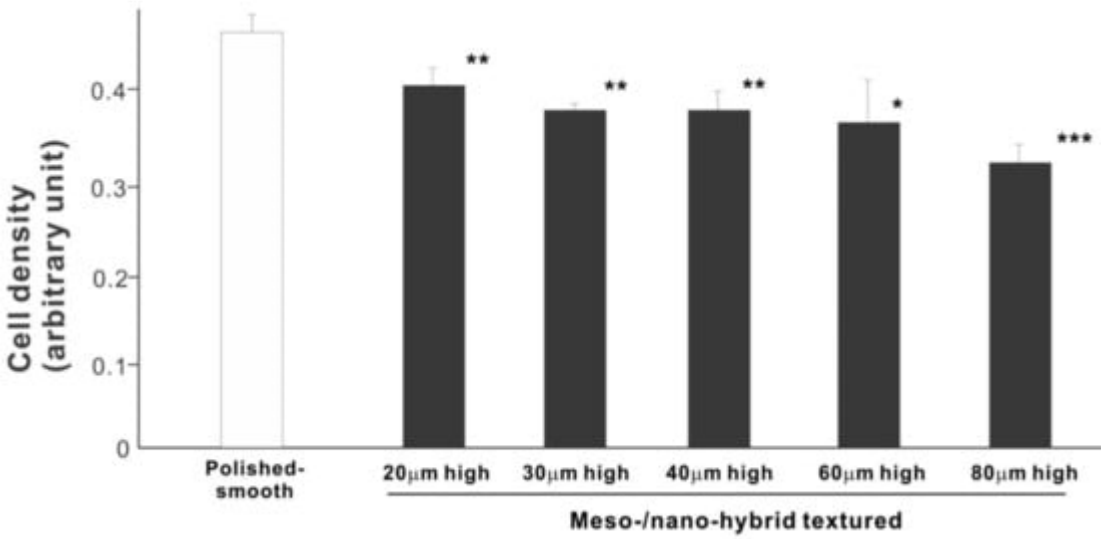

Figure 6. Proliferation of osteoblasts, measured as cell density, on differently textured zirconia surfaces, evaluated by the WST-1 assay on day 5. * $p < 0.05$, ** $p < 0.01$, *** $p < 0.001$, statistically significant difference compared with a polished surface.

5. Osteoblast Differentiation on Meso-/Nano-Scale Hybrid Textured Zirconia

We next examined osteoblastic differentiation by measuring ALP activity, matrix mineralization ability, and the expression levels of osteoblastic differentiation marker genes. Unlike the results in the cell attachment and cell density assays, the ALP activity measured on day 10 was significantly higher for all meso-/nano-scale hybrid textured zirconia than on the polished surface (histogram in **Figure 7**). There was a disproportional change of ALP activity relative to the spike height, with the ALP activity being the highest when the spikes were 40 μm high. The result of ALP staining of the culture confirmed these results (top images in **Figure 7**). The matrix calcium deposition measured on day 20 also dominated on the hybrid surfaces and seemed to increase linearly with the spike height up to a certain point, followed by a decline (**Figure 8**). Specifically, the peak of the calcium deposition was found with 40 μm-high spikes.

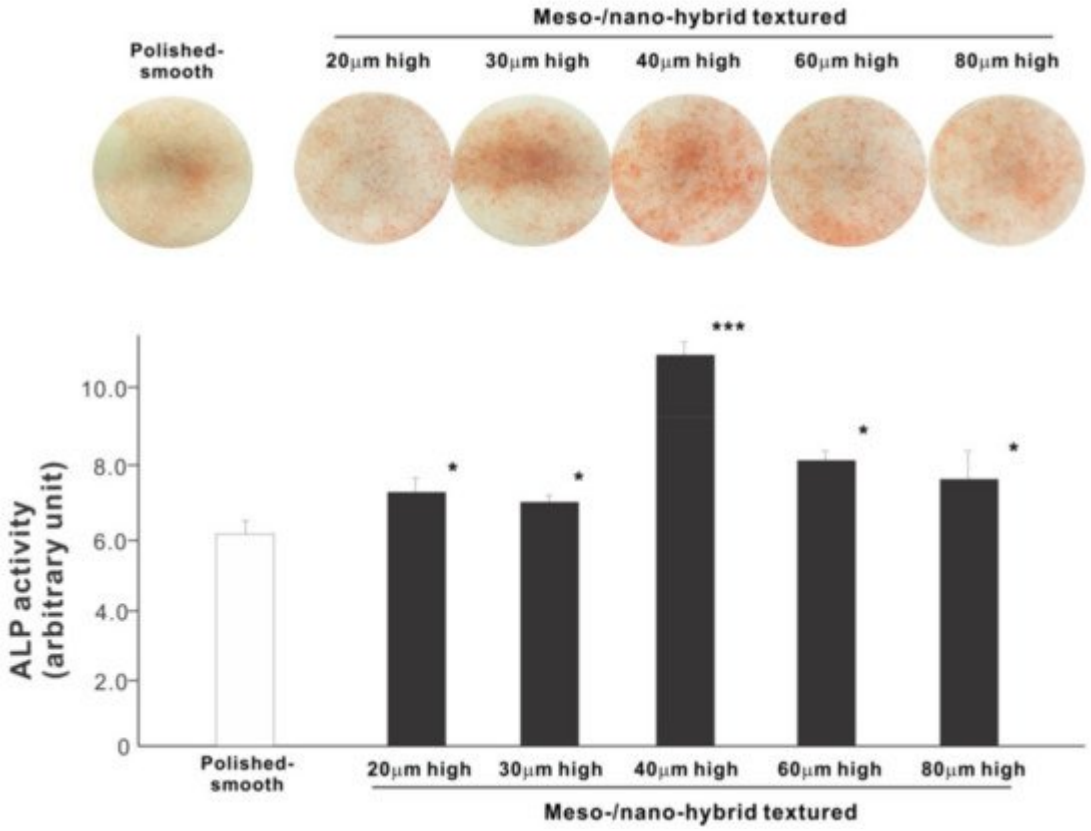

Figure 7. Osteoblastic differentiation on variously textured zirconia surfaces evaluated by alkaline phosphatase (ALP) activity on day 10 of culture. Culture images after ALP staining (top images) and the amount of ALP (histogram) measured by chemical detection are presented. * $p < 0.05$, *** $p < 0.001$, statistically significant difference compared with a polished surface.

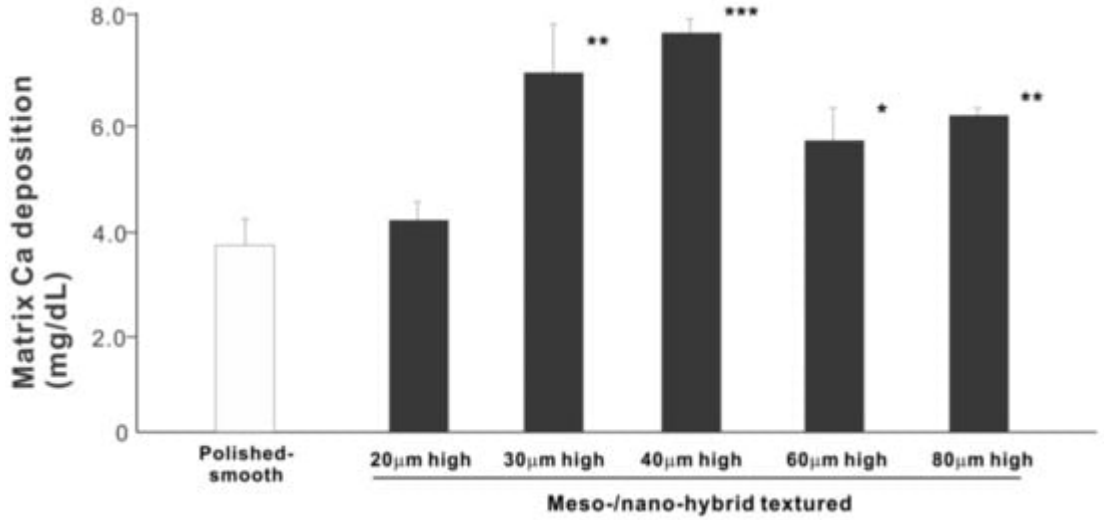

Figure 8. Osteoblastic differentiation on variously textured zirconia surfaces evaluated by matrix calcium deposition on day 15 of culture. * $p < 0.05$, ** $p < 0.01$, *** $p < 0.001$, statistically significant difference compared with a polished surface.

The results of real-time PCR resembled those of the matrix calcium deposition (**Figure 9**). The expression of collagen type 1 gene, an early-stage osteoblastic marker, was generally upregulated on the hybrid surfaces compared with the polished surface throughout the culture period. The expression level increased with the height of meso-spikes and was the highest with 40 μm-high spikes at all time points tested. The expression of osteocalcin, a late-stage osteoblastic marker, was significantly higher on the hybrid surfaces and most upregulated on the 40 μm-high spiked surface.

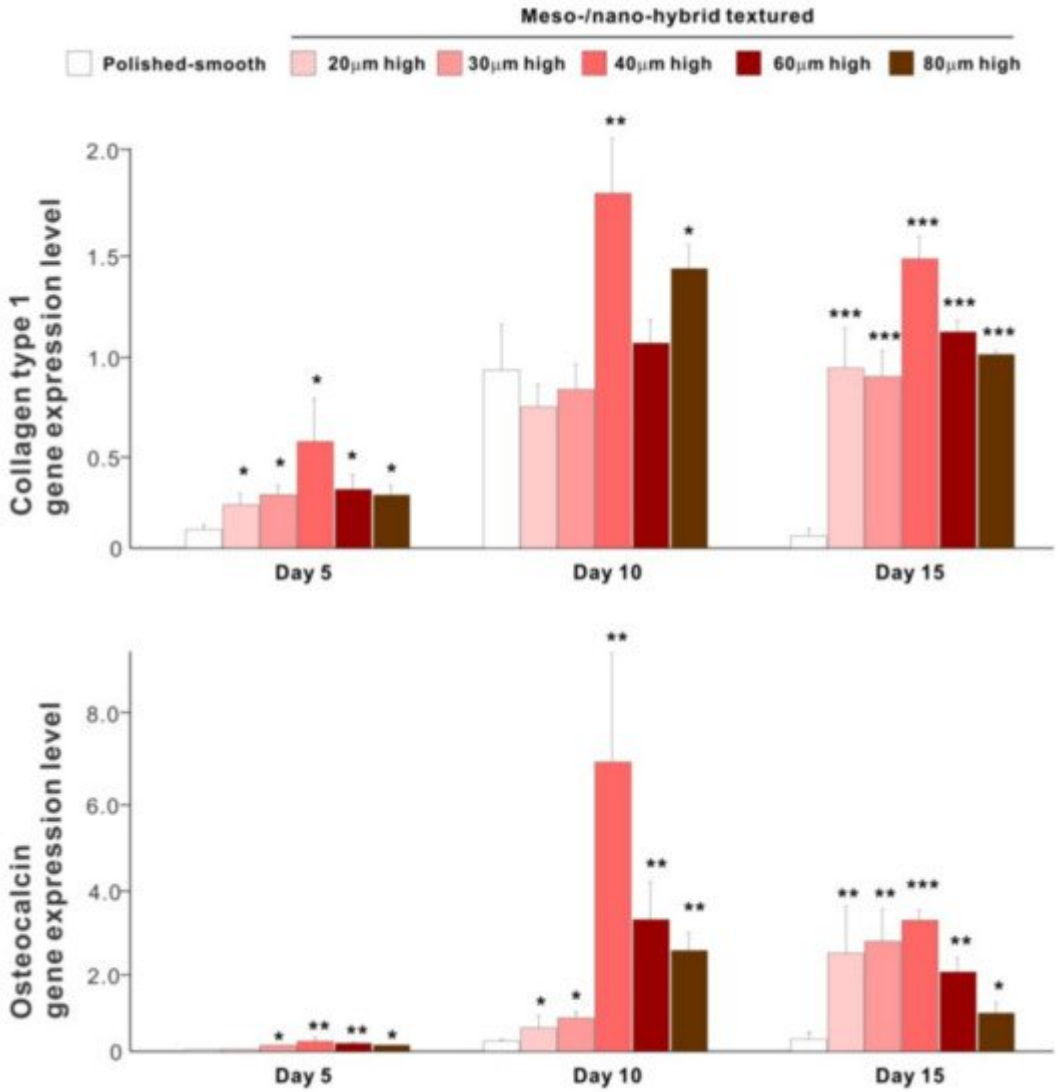

Figure 9. Osteoblastic differentiation on variously textured zirconia surfaces evaluated by real-time PCR on days 5, 10, and 15 of culture. Collagen type 1 and osteocalcin gene expression were evaluated as early- and late-stage differentiation markers, respectively. * $p < 0.05$, ** $p < 0.01$, *** $p < 0.001$, statistically significant difference compared with a polished surface.

6. In Vivo Bone-and-Implant Integration

The biomechanical strength of bone–implant integration is the most critical and relevant factor for evaluating the performance of an implant as a load-anchoring device. The strength of bone–implant integration assessed by biomechanical push-in testing at an early stage of healing, two weeks post-implantation, was considerably higher for all meso-/nano-scale hybrid textured implants than the polished-smooth implants (**Figure 10**A). The push-in values increased with the spike height until the spikes reached 40 μm high and plateaued afterward. The push-in value for implants with 40 μm-high spikes was 8 times greater than for the polished implants. It was also noteworthy that the bone integration of 40 μm-high spiked implants was over twice that of 20 μm-high spiked implants. Similarly, during the later stages of healing, after four weeks, the push-in values for the hybrid-textured

implants far exceeded that of the polished implants (**Figure 10**B). The greatest push-in value was noted for the implants with 40 μm-high spikes, dominating the values of the polished implants and 20 μm-spiked implants by 7 and 3.5 times, respectively.

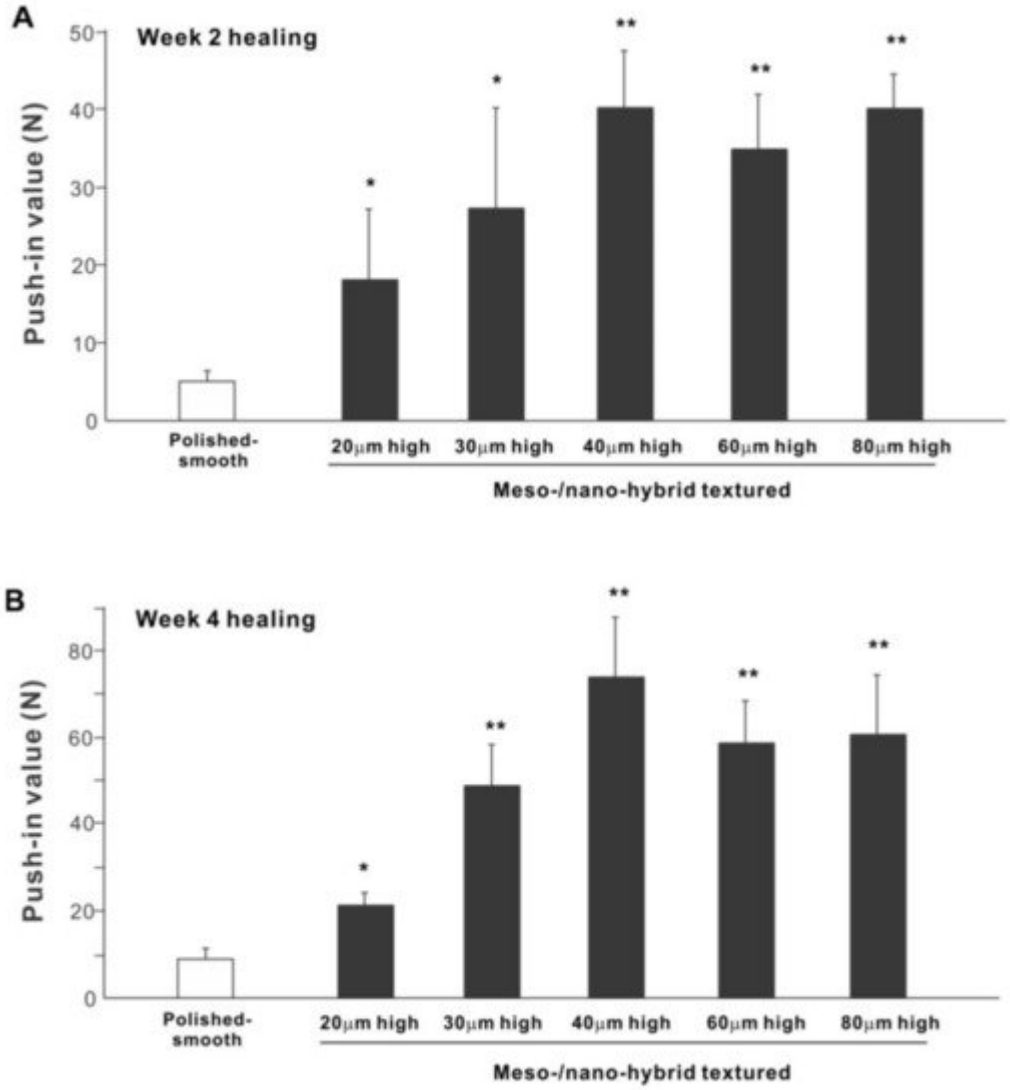

Figure 10. The biomechanical push-in test in the rat femur model at week 2 (**A**) and 4 (**B**) post-implantation. * $p < 0.05$, ** $p < 0.01$, statistically significant difference compared with a polished-smooth surface.

To verify the bone formation around zirconia implants, selected implants were examined for tissue morphology and chemistry after push-in testing (**Figure 11**). The hybrid-textured implants with 40 μm-high spikes were extensively covered with biological structures, as shown in the SEM image. The structures in the top half of the implant originated from the innate cortical bone and/or periosteum and spread to the implant surface, whereas the ones on the bottom half appeared to have stemmed from the implant interface within the bone marrow. The majority of the biological structures were positive for Ca and P signals in the elemental mapping, providing evidence that there was extensive bone formation around the implant.

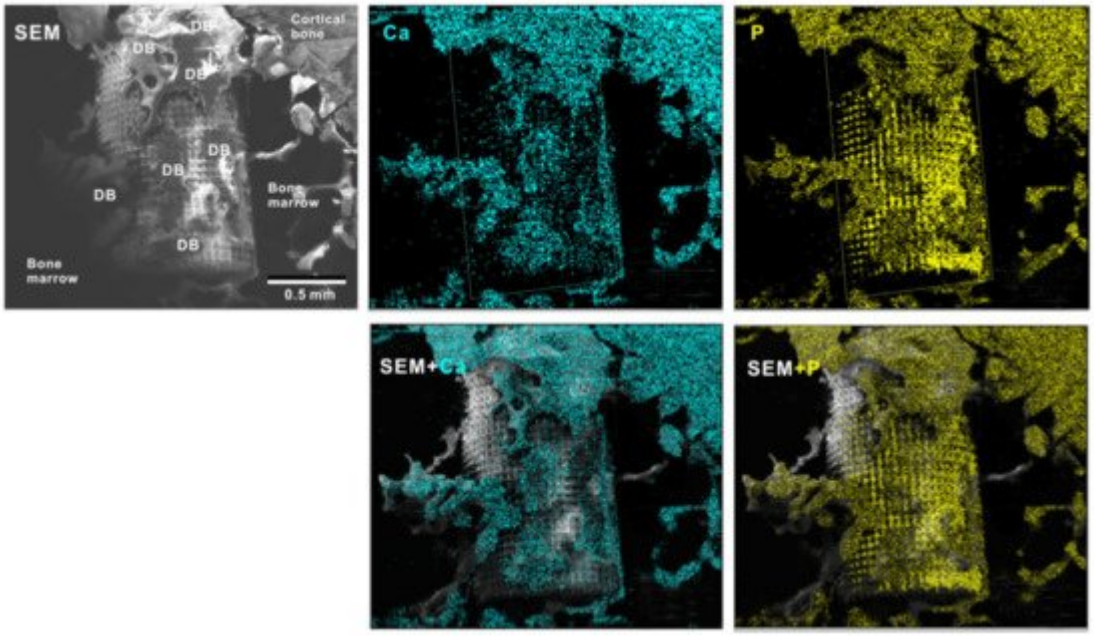

Figure 11. Peri-implant tissue morphology and chemistry around a zirconia implant. To verify bone formation around implants, selected implants were analyzed after the push-in test. A representative result from a meso-/nano-scale hybrid textured implant with 40 μm-high spikes is presented here. SEM images and elemental mapping for Ca and P signals as well as their superimposed images are shown.

7. Technology Validation for Clinical Translation

To overcome potential challenges in creating the bio-inspired meso-/nano-scale hybrid textured zirconia surface on future medical devices, a prototype dental implant for human use was developed. The prototype, which was 4 mm in diameter and 10 mm in length, was screw-shaped with macroscopic helical threads to represent a size and shape standard for dental implants. Solid-state laser etching was applied to form 40 μm-high spikes as optimized in the experiments described above. Low-magnification SEM images depicted uniform and seamless formation of cactus-inspired meso-spikes all over the threaded implant surface (**Figure 12**A–C). There were no visible irregularities or defects in the spikes in any areas (i.e., peak, flank, and valley regions) of the macroscopic threads. The spikes created a controlled, oscillating configuration with a repetitive, peak-and-valley pattern. High-magnification images confirmed the formation of fully networked nano-trabeculae, just as seen on experimental samples, evenly and consistently appearing all over the implant surface (**Figure 12**D,E).

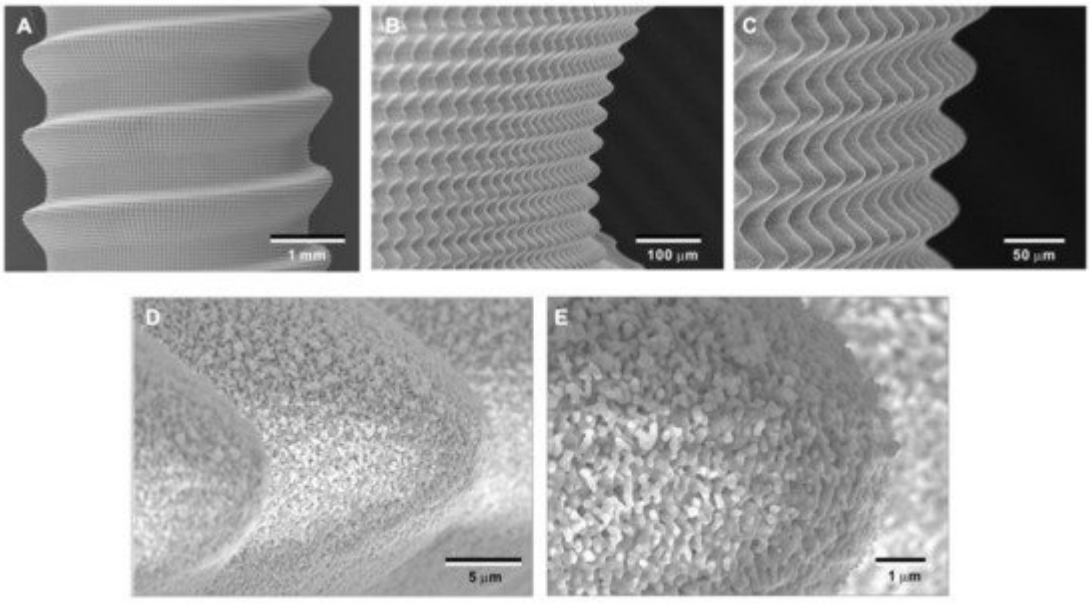

Figure 12. Prototype development of a medical device with the bio-inspired meso-/nano-scale hybrid textured surface for human applications. To verify the viability of the laser technology introduced here in creating medical devices, a zirconia dental implant was developed. A screw-shaped implant, made from Y-TZP, was formed to represent a standardly sized and shaped dental implant with macroscopic helical threads (**A**). After laser etching, the implant vividly presents cactus-inspired meso-spikes (**B**,**C**) and trabecular bone-like nano-scale interwoven architecture (**D**,**E**).

References

1. Shao, F.; Wu, Y.; Tian, Z.; Liu, S. Biomimetic nanoreactor for targeted cancer starvation therapy and cascade amplificated chemotherapy. Biomaterials 2021, 274, 120869.
2. Wang, X.; Gao, B.; Chan, B.P. Multiphoton microfabrication and micropatterning (MMM)—An all-in-one platform for engineering biomimetic soluble cell niches. Biomaterials 2021, 269, 120644.
3. Bai, J.; Wang, H.; Chen, H.; Ge, G.; Wang, M.; Gao, A.; Tong, L.; Xu, Y.; Yang, H.; Pan, G.; et al. Biomimetic osteogenic peptide with mussel adhesion and osteoimmunomodulatory functions to ameliorate interfacial osseointegration under chronic inflammation. Biomaterials 2020, 255, 120197.
4. Zhu, Y.; Kong, L.; Farhadi, F.; Xia, W.; Chang, J.; He, Y.; Li, H. An injectable continuous stratified structurally and functionally biomimetic construct for enhancing osteochondral regeneration. Biomaterials 2019, 192, 149–158.
5. Wang, T.; Zhai, Y.; Nuzzo, M.; Yang, X.; Yang, Y.; Zhang, X. Layer-by-layer nanofiber-enabled engineering of biomimetic periosteum for bone repair and reconstruction. Biomaterials 2018, 182, 279–288.

6. Zhou, X.; Sahai, N.; Qi, L.; Mankoci, S.; Zhao, W. Biomimetic and nanostructured hybrid bioactive glass. Biomaterials 2015, 50, 1–9.
7. Fritschen, A.; Blaeser, A. Biosynthetic, biomimetic, and self-assembled vascularized Organ-on-a-Chip systems. Biomaterials 2021, 268, 120556.
8. Holzwarth, J.M.; Ma, P.X. Biomimetic nanofibrous scaffolds for bone tissue engineering. Biomaterials 2011, 32, 9622–9629.
9. Yamada, M.; Ueno, T.; Tsukimura, N.; Ikeda, T.; Nakagawa, K.; Hori, N.; Suzuki, T.; Ogawa, T. Bone integration capability of nanopolymorphic crystalline hydroxyapatite coated on titanium implants. Int. J. Nanomed. 2012, 7, 859–873.
10. Tsukimura, N.; Ueno, T.; Iwasa, F.; Minamikawa, H.; Sugita, Y.; Ishizaki, K.; Ikeda, T.; Nakagawa, K.; Yamada, M.; Ogawa, T. Bone integration capability of alkali- and heat-treated nanobimorphic Ti–15Mo–5Zr–3Al. Acta Biomater. 2011, 7, 4267–4277.
11. Tsukimura, N.; Yamada, M.; Iwasa, F.; Minamikawa, H.; Att, W.; Ueno, T.; Saruwatari, L.; Aita, H.; Chiou, W.-A.; Ogawa, T. Synergistic effects of UV photofunctionalization and micro-nano hybrid topography on the biological properties of titanium. Biomaterials 2011, 32, 4358–4368.
12. Ueno, T.; Tsukimura, N.; Yamada, M.; Ogawa, T. Enhanced bone-integration capability of alkali- and heat-treated nanopolymorphic titanium in micro-to-nanoscale hierarchy. Biomaterials 2011, 32, 7297–7308.
13. Kubo, K.; Tsukimura, N.; Iwasa, F.; Ueno, T.; Saruwatari, L.; Aita, H.; Chiou, W.-A.; Ogawa, T. Cellular behavior on TiO2 nanonodular structures in a micro-to-nanoscale hierarchy model. Biomaterials 2009, 30, 5319–5329.
14. Hori, N.; Iwasa, F.; Ueno, T.; Takeuchi, K.; Tsukimura, N.; Yamada, M.; Hattori, M.; Yamamoto, A.; Ogawa, T. Selective cell affinity of biomimetic micro-nano-hybrid structured TiO2 overcomes the biological dilemma of osteoblasts. Dent. Mater. 2010, 26, 275–287.
15. Hori, N.; Iwasa, F.; Tsukimura, N.; Sugita, Y.; Ueno, T.; Kojima, N.; Ogawa, T. Effects of UV photofunctionalization on the nanotopography enhanced initial bioactivity of titanium. Acta Biomater. 2011, 7, 3679–3691.
16. Iwasa, F.; Tsukimura, N.; Sugita, Y.; Kanuru, R.K.; Kubo, K.; Hasnain, H.; Att, W.; Ogawa, T. TiO2 micro-nano-hybrid surface to alleviate biological aging of UV-photofunctionalized titanium. Int. J. Nanomed. 2011, 6, 1327–1341.
17. Miyauchi, T.; Yamada, M.; Yamamoto, A.; Iwasa, F.; Suzawa, T.; Kamijo, R.; Baba, K.; Ogawa, T. The enhanced characteristics of osteoblast adhesion to photofunctionalized nanoscale TiO2 layers on biomaterials surfaces. Biomaterials 2010, 31, 3827–3839.

18. Ogawa, T.; Saruwatari, L.; Takeuchi, K.; Aita, H.; Ohno, N. Ti Nano-nodular Structuring for Bone Integration and Regeneration. J. Dent. Res. 2008, 87, 751–756.
19. Sugita, Y.; Ishizaki, K.; Iwasa, F.; Ueno, T.; Minamikawa, H.; Yamada, M.; Suzuki, T.; Ogawa, T. Effects of pico-to-nanometer-thin TiO2 coating on the biological properties of microroughened titanium. Biomaterials 2011, 32, 8374–8384.
20. Rezaei, N.M.; Hasegawa, M.; Ishijima, M.; Nakhaei, K.; Okubo, T.; Taniyama, T.; Ghassemi, A.; Tahsili, T.; Park, W.; Hirota, M.; et al. Biological and osseointegration capabilities of hierarchically (meso-/micro-/nano-scale) roughened zirconia. Int. J. Nanomed. 2018, 13, 3381–3395.
21. Att, W.; Tsukimura, N.; Suzuki, T.; Ogawa, T. Effect of supramicron roughness characteristics produced by 1- and 2-step acid etching on the osseointegration capability of titanium. Int. J. Oral Maxillofac. Implant. 2007, 22, 719–728.
22. Ogawa, T.; Nishimura, I. Different bone integration profiles of turned and acid-etched implants associated with modulated expression of extracellular matrix genes. Int. J. Oral Maxillofac. Implant. 2003, 18, 200–210.
23. Ogawa, T.; Nishimura, I. Genes Differentially Expressed in Titanium Implant Healing. J. Dent. Res. 2006, 85, 566–570.
24. Ogawa, T.; Ozawa, S.; Shih, J.-H.; Ryu, K.; Sukotjo, C.; Yang, J.-M.; Nishimura, I. Biomechanical Evaluation of Osseous Implants Having Different Surface Topographies in Rats. J. Dent. Res. 2000, 79, 1857–1863.
25. Ozawa, S.; Ogawa, T.; Iida, K.; Sukotjo, C.; Hasegawa, H.; Nishimura, R.; Nishimura, I. Ovariectomy hinders the early stage of bone-implant integration: Histomorphometric, biomechanical, and molecular analyses. Bone 2002, 30, 137–143.
26. Tsukimura, N.; Kojima, N.; Kubo, K.; Att, W.; Takeuchi, K.; Kameyama, Y.; Maeda, H.; Ogawa, T. The effect of superficial chemistry of titanium on osteoblastic function. J. Biomed. Mater. Res. Part A 2008, 84, 108–116.
27. Nakamura, H.; Saruwatari, L.; Aita, H.; Takeuchi, K.; Ogawa, T. Molecular and Biomechanical Characterization of Mineralized Tissue by Dental Pulp Cells on Titanium. J. Dent. Res. 2005, 84, 515–520.
28. Nakamura, H.; Shim, J.; Butz, F.; Aita, H.; Gupta, V.; Ogawa, T. Glycosaminoglycan degradation reduces mineralized tissue–titanium interfacial strength. J. Biomed. Mater. Res. Part A 2006, 77, 478–486.
29. Nakamura, H.; Butz, F.; Saruwatari, L.; Ogawa, T. A role for proteoglycans in mineralized tissue-titanium adhesion. J. Dent. Res. 2007, 86, 147–152.

30. Takeuchi, K.; Saruwatari, L.; Nakamura, H.K.; Yang, J.-M.; Ogawa, T. Enhanced intrinsic biomechanical properties of osteoblastic mineralized tissue on roughened titanium surface. J. Biomed. Mater. Res. Part A 2005, 72, 296–305.
31. Butz, F.; Aita, H.; Wang, C.; Ogawa, T. Harder and Stiffer Bone Osseointegrated to Roughened Titanium. J. Dent. Res. 2006, 85, 560–565.
32. Butz, F.; Ogawa, T.; Chang, T.-L.; Nishimura, I. Three-dimensional bone-implant integration profiling using micro-computed tomography. Int. J. Oral Maxillofac. Implant. 2006, 21, 687–695.
33. Att, W.; Takeuchi, M.; Suzuki, T.; Kubo, K.; Anpo, M.; Ogawa, T. Enhanced osteoblast function on ultraviolet light-treated zirconia. Biomaterials 2009, 30, 1273–1280.